RESEARCH PAPER

Application of Central Composite Design for Optimizing Mechanical Performance of Geopolymer Paste from Fly Ash Using the Mechanosynthesis Method: Structural and Microstructural Analysis

Yassine El Maataoui[1] · Saliha Alehyen[1] · Mouhcine Fadil[2] · Badr Aouan[1] · Ahmed Liba[3] · Hamid Saufi[1] · M'hamed Taibi[1]

Abstract

This research aims to optimize the mechanical performance of a geopolymer paste derived from fly ash (FA) using the Central Composite Design (CCD) method. The study also explores mechanosynthesis as a modern technique to create a pre-geopolymer powder, which is then used to develop the paste. Key factors considered include grinding speed and duration, curing time and temperature, and NaOH concentration. Twenty-nine geopolymer pastes were prepared based on the CCD experimental matrix, and their compressive strength (MPa) and bulk density (g/cm^3) were measured after 28 days of ambient solidification. The structural properties of the raw materials and resulting geopolymer samples were analyzed using X-ray diffraction (XRD) and Fourier-transform infrared (FTIR) spectroscopy. Morphological characteristics were examined with Scanning Electron Microscopy (SEM) and Energy-Dispersive X-ray (EDX) spectroscopy. The compressive strength of the samples ranged from 11.22 to 32.41 MPa, while bulk density varied from 1.31 to 1.62 g/cm^3. The optimized conditions for the highest-performing geopolymer paste (46.47 MPa and 1.64 g/cm^3) were identified as a grinding speed of 300 rpm, grinding time of 15 min, curing time of 24 h, curing temperature of 80 °C, and a NaOH concentration of 10 M. The performant geopolymer paste demonstrated a low-porosity structure primarily composed of dense amorphous sodium aluminosilicate gel. Future research could explore the application of different raw materials and additives to enhance the properties of geopolymer pastes further. Additionally, investigating the long-term durability and environmental impact of these materials can provide deeper insights into their potential for sustainable construction applications.

Keywords Geopolymers · Mechanosynthesis · Optimization · Central composite design · Compressive strength · Fly ash

Abbreviations

CCD	Central composite design
FA	Fly ash
PGP	Pre-geopolymer powder
RPM	Round per min
G	Geopolymer
DF	Degree of freedom
XRF	X-ray fluorescence
XRD	X-ray diffraction
FTIR	Fourier transform infrared
SEM	Scanning electron microscopy
EDS	Energy dispersive spectroscopy
PSD	Particle size distribution

✉ Yassine El Maataoui
yassine_elmaataoui2@um5.ac.ma

1 Laboratory of Physics and Chemistry of Inorganic and Organic Materials (LPCMIO), Materials Science Research Center (CSM), Mohammed V University in Rabat, Ecole Normale Supérieure (ENS), Rabat, Morocco

2 Laboratory of Applied Organic Chemistry, Faculty of Sciences and Techniques, Sidi Mohamed Ben Abdellah University, Road of Imouzzer, P.O. Box 2202, Fez, Morocco

3 Laboratory of Energetic and Materials Engineering, Faculty of Sciences and Technologies, Sultan Moulay Slimane University, BP 523, 23000 Beni Mellal, Morocco

1 Introduction

Geopolymers present environmentally friendly materials that could be used as promising alternatives to Portland cement in the construction sector. Indeed, the production of one ton

of cement leads to the emission of approximately one ton of carbon dioxide, which is one of the main contributors to global warming as it escapes into the air (Sathsarani et al. 2023).

Geopolymers offer excellent performance as building materials, owing to their good mechanical, thermal, chemical, and electrical properties, as well as their low synthesis energy, making them economical products (Davidovits 1991; Tang et al. 2023). It is important to mention that aluminosilicate-rich precursors represent the basic feedstocks for the synthesis of geopolymers, and can be natural resources or industrial wastes. The metakaolin derived from the calcination of kaolin clay represents one of the most important materials adopted as a source of aluminosilicates for geopolymer formulation, due to its high reactivity with an alkaline activating solution (Archer de Carvalho et al. 2024; Barbosa et al. 2000; Duxson et al. 2007; Tchadjie & Ekolu 2018; Van Jaarsveld & Van Deventer 1999). On the other hand, industrial waste recycling represents another source of aluminosilicates, such as blast furnace slag obtained from steel complexes(Lecomte et al. 2003), and FA from coal-fired power plants(Van Jaarsveld & Van Deventer 1999), and red mud from a by-product of the Bayer process(Panda et al. 2024).

Recently, attention has focused on finding new methods of synthesizing geopolymers without requiring direct contact with dangerous alkaline solutions while simultaneously obtaining a product that has the same form as OPC in powder form and can be easily mixed with water (Singh & Middendorf 2020).

As a result, the development of a pre-geopolymer powder (PGP) using mechanosynthesis technology was proposed, The PGP refers to the precursor material mixture prepared before the geopolymerization process. According to the literature, mechanosynthesis is a high-energy ball milling process in which raw materials are mixed in the solid state and transformed into a homogeneous powder of small particle size. This technology increases the surface of interaction between particles of fly ash with the alkaline activator, leading to more complete and efficient reactions, and a more uniform particle size distribution (PSD) (Ahmed et al. 2023; Özkılıç et al. 2023). This grinding process is carried out by a mechanical ball mill consisting of a container made of different materials (such as hardened steel, tungsten carbide, garnet, zirconium oxide, silicon nitride, and stainless steel) and containing grinding balls of different sizes formed from specific substances. Grinding time and speed are important factors influencing the particle size of the PGP and hence the physical and mechanical properties of the derived paste (Bouchenafa et al. 2019; Hamzaoui et al. 2004). Wei et al. developed an intelligent mix design method for fly ash-based

geopolymer, aiming to meet the strength, cost, and environmental protection requirements. Their study introduces a multiobjective design optimization method (Dong et al. 2023). While each study adopts different methodologies and precursor combinations, they collectively underscore the significance of mixture design in optimizing geopolymer synthesis for superior mechanical properties (Luan et al. 2022).

Moreover, geopolymers possess distinctive characteristics that make them suitable for specific applications. They feature high heat and fire resistance, making them suitable for high-temperature environments. Additionally, they offer high mechanical strength and high durability, making them suitable for civil engineering applications (Al-Fakih et al. 2023).

Geopolymer technology research continues, but much still needs to be discovered regarding optimal manufacturing processes and applications for geopolymers. However, the potential advantages of this technology make it an alternative field of research and development (Nawaz et al. 2020; Pradhan et al. 2024a, b).

The absence of industry standards and norms presents a difficulty for the common approval of geopolymer technology. Ensuring the quality and consistency of geopolymer materials could prove challenging without defined guidelines for manufacturing and testing. In addition, in some circumstances, the manufacturing costs may exceed those of conventional cement-based products, potentially acting as a deterrent to widespread approval (Habert et al. 2011; Martínez & Miller 2023).

In addition to these constraints, the development of geopolymer technology can significantly improve the environmental impact of the construction sector while providing high-performance materials for a large variety of applications. As research and development in this field continue, geopolymer materials are expected to increase in use in the future (Bajpai et al. 2020).

Despite their promising properties, particularly in the construction area, the widespread use of geopolymers is currently limited. As a result, geopolymer is primarily employed in prefabricated materials such as paving stones, paving slabs, and bricks. To broaden the application scope of these materials, novel manufacturing methods must be introduced. One such promising method is the "mechanosynthesis" process, which involves fine grinding of precursors (Mucsi et al. 2015). Although the geopolymerization process is usually carried out by mixing aluminosilicate raw materials with alkaline liquids, in this context a mechanosynthesis process using an alkaline activator as a powder is proposed to elaborate a geopolymer material that can be easily used (Gaffet et al. 1999).

Various approaches utilizing different design methods have been explored to optimize the synthesis of

high-performance geopolymers including Artificial intelligence (AI) methods (Parhi et al. 2024; Pradhan, Panda, Parhi, et al. 2024). Kanagaraj et al. investigated optimizing the mix proportion of High Strength Alkali Activated Concrete (HSAAC) using the Taguchi Method (TM) (Kanagaraj et al. 2022). The present study focused on applying the CCD approach to optimize various factors such as grinding speed, grinding duration, curing time, curing temperature, and NaOH concentration in fly ash-based geopolymer production via the mechanosynthesis process (Wang & Fan 2021). To evaluate the influence of different parameters on compressive strength and density, many investigations have been performed with different aluminosilicate precursors and mixture designs (Driouich et al. 2023). Lulseged et al. used the Taguchi model to find the optimal geopolymer with fly ash. Various parameters were tested, minimizing experimentation while maximizing the compressive strength. With a Maximum of 24.96 MPa for compressive strength and 4.40 MPa for splitting tensile strength (Addis et al. 2023), Zerzouri et al. compared conventional geopolymers with those obtained through mechanosynthesis, highlighting structural and mechanical differences, achieving compressive strengths of 28 MPa compared to 15 MPa for conventional geopolymer pastes (Zerzouri et al. 2021). All these experiential methods offer distinct advantages depending on the research objectives. The CCD is efficient in optimization and captures complex interactions and quadratic effects, making it valuable for geopolymer optimization. BBD focuses on quadratic models, making it suitable for optimization without exploring extreme conditions. The Taguchi method excels at early screening and improving robustness with the fewest number of experiments by focusing on main effects rather than interactions (Ghafri et al. 2024).

This study aimed to optimize the mechanical properties of a fly ash-derived geopolymer paste by applying the central composite design methodology. The research delves into mechanosynthesis as a modern technique to produce pre-geopolymer powders (PGP) for developing geopolymer pastes. A thorough investigation of key parameters, including grinding speed and duration, curing time and temperature, and NaOH concentration, was conducted to identify the optimal conditions for achieving superior mechanical performance. The raw materials, pre-geopolymer powders, and geopolymer pastes were subjected to extensive physicochemical analyses to ensure a detailed and comprehensive evaluation. This study's experimental and analytical approach seeks to uncover the best synthesis conditions for enhancing the mechanical properties of geopolymer pastes, providing valuable insights for future applications.

2 Materials and Methods

2.1 Materials

In this study, three solid components were employed as raw materials. The Fly ash powder was collected from a coal-fired power plant in the Jorf Lasfar region of Morocco, (Dhole, 2020; Wang et al., 2016), the sodium hydroxide pellets of 99% purity imported from the Cadillac Company, and the crystalline sodium silicate granules with 99% purity were also imported from Cadillac. The chemical composition determined by X-ray fluorescence (XRF) spectroscopy was performed using the STDHX8000CIM XRF analyzer. This instrument provides highly accurate measurements with a detection limit of 0.01% for major elements and 0.001% for trace elements. Moreover, Table 1 indicated that FA used from the Jorf Lasfar region of Morocco is a rich aluminosilicate precursor because the percentage of $SiO_2 + Al_2O_3 + Fe_2O_3$ combined exceeded 70% these oxides are essential in the geopolymerization process. When the percentage of CaO is less than 10%, the FA is classified as class F (Dhole, 2020; Wang et al., 2016). Variations in fly ash composition from different sources can have significant effects on the compression and density of the geopolymer. However, the presence of impurities, higher calcium, and variations in the SiO_2/Al_2O_3 ratio can influence the consistency and performance of the geopolymer (Kakasor Ismael Jaf et al. 2023).

2.2 Method

2.2.1 Geopolymer Synthesis

The mechanosynthesis technique was chosen to produce PGP based on FA, NaOH, and Na_2SiO_3. The formulation, milling, and processing parameters were simultaneously adjusted to optimize the quality of these powders and thus the performance of the resulting pastes. These powders were subsequently used to formulate geopolymer pastes through the addition of water. The selection of these parameters was guided by a combination of literature insights, and statistical analysis including regression modeling and analysis of variance (ANOVA), which helped in identifying the most

Table 1 Chemical composition of fly ash according to XRF

Constituants	SiO$_2$	Al$_2$O$_3$	Fe$_2$O$_3$	CaO	MgO	SO$_3$	K$_2$O	P$_2$O$_5$	MnO	TiO$_2$
% weight	48.04	23.61	11.09	6.10	1.02	0.17	3.17	3.17	0.03	1.43

influential parameters and their optimal settings (Emad et al. 2022).

A CCD design with three replicates was used to produce geopolymers with suitable qualities. This optimization process involved adjusting various parameters such as grinding speed grinding duration, curing time, curing temperature, and NaOH concentration. Based on the results of previous studies, the (FA)/ (AA) and Na_2SiO_3/NaOH mass ratios were fixed at 2.5 (Alloun et al. 2023; Zerzouri et al. 2021).

According to this optimization process, the quantity of all the mixed raw materials: FA 100 gr, NaOH 11.43 gr, Na_2SiO_3 28.57 gr, water 28.57 ml, 21.98 ml, 17.85 ml, for NaOH concentration 10M, 13M, and 16M, respectively.

The synthesis of the geopolymer by mechanosynthesis following CCD was performed using a high-energy planetary ball mill (Pulverizette 6, Fritsch) to grind the raw materials (FA, NaOH., and Na_2SiO_3). Then the powder was mixed with water and mold. After 28 days of drying at atmospheric pressure, the compressive strength properties and density of the 29 prepared geopolymer pastes were evaluated. The results were subsequently analyzed to determine the optimum settings using the CCD methodology.

2.2.2 Experiment Design, Statistical Analysis, and Optimization Process

2.2.2.1 Central Composite Design
The experimental CCD was used to streamline the number of experiments and evaluate the influence of various parameters on the selected responses. The factors studied included the grinding speed, grinding time, curing time, curing temperature, and NaOH concentration these factors are listed in Table 2, along with their associated coding and selected levels.

This design involved five factors with three repetitions in the middle of the domain, culminating in 29 experiments (Srinivasa et al. 2023). Applying the CCD to the factors mentioned above at their three levels created a matrix of experiments comprising 29 different combinations, as shown in Table 3.

The CCD offers efficient optimization by allowing the estimation of both the main effects and quadratic effects of factors,

Table 2 The factors and levels applied in CCD

Factors	Symbol	Unity	Factors levels		
			−1	0	1
Grinding time	X_1	Minutes	5	10	15
Grinding speed	X_2	RPM	300	350	400
NaOH concentration	X_3	mol/L	10	13	16
Curing time	X_4	Hours	12	24	48
Curing temperature	X_5	°C	24	52	80

Table 3 Matrix of the 29 experiments generated by the CCD

Experiment series	X_1	X_2	X_3	X_4	X_5
1	−1	−1	−1	−1	0
2	−1	−1	−1	1	−1
3	1	−1	−1	1	0
4	1	−1	−1	−1	−1
5	−1	1	−1	1	0
6	−1	1	−1	−1	−1
7	1	1	−1	−1	0
8	1	1	−1	1	−1
9	−1	−1	1	1	0
10	−1	−1	1	−1	−1
11	1	−1	1	−1	0
12	1	−1	1	1	−1
13	−0	1	1	−1	0
14	−1	1	1	1	−1
15	1	1	1	1	0
16	1	1	1	−1	−1
17	0	0	−1	0	1
18	0	0	1	0	1
19	0	−1	0	0	1
20	0	1	0	0	1
21	−1	0	0	0	1
22	1	0	0	0	1
23	0	0	0	0	0
24	0	0	0	0	−1
25	0	0	0	−1	1
26	0	0	0	1	1
27	0	0	0	0	1
28	0	0	0	0	1
29	0	0	0	0	1

allowing the identification of optimal experimental conditions in a relatively small number of experiments (Ferreira et al. 2007).

According to the CCD, geopolymer powder can be produced in eight distinct ways, considering that only two parameters influence the particle size of the powder: grinding speed (GS) and grinding time (GT). These powders are essentially a mixture of spherical solid, hollow, and vitreous particles of different sizes and shapes (Goodarzi & Sanei 2009).

2.2.2.2 Statistical Analysis
In this study, a 2nd-order polynomial regression model was used to analyze the relationships between the various factors studied (X_1–X_5) and the targeted response (Y) (Ahmad & Basu 2024). The proposed model is represented by the following equation Eq. (1):

$$\begin{aligned}
Y = {} & b_0 + b_1X_1 + b_2X_2 + b_3X_3 + b_4X_4 \\
& + b_5X_5 + b_{11}X_1X_1 + b_{22}X_2X_2 + b_{33}X_3X_3 \\
& + b_{44}X_4X_4 + b_{55}X_5X_5 + b_{12}X_1X_2 + b_{13}X_1X_3 \\
& + b_{23}X_2X_3 + b_{14}X_1X_4 + b_{24}X_2X_4 + b_{34}X_3X_4 \\
& + b_{15}X_1X_5 + b_{25}X_2X_5 + b_{35}X_3X_5 + b_{45}X_4X_5 + \varepsilon
\end{aligned} \tag{1}$$

This model comprises various parameters to predict the response. The intercept term (b_0) represents the theoretical mean response when all influencing factors are absent. Additionally, linear coefficients (b_1–b_5) signify the direct impact of each factor on the response. Quadratic terms (b_{11}–b_{55}) account for the curvature in the relationship between factors and response, allowing for nonlinear effects. Interaction terms (b_{12}–b_{45}) capture the joint influence of two factors on the response. An error term (ε) is also included to account for unexplained variability in the data.

The analysis was conducted using JMP (version 16) software and DESIGN EXPERT (version 16) software, which facilitated regression analysis and graphical visualization of the data. Additionally, software was used to determine the optimal conditions of the factors by solving the regression equations and generating, and interpreting the response surface plots.

2.2.2.3 Optimization Tools The iso-response profile in 2D and 3D, as well as the desirability profile, are powerful tools in the field of experimental design and optimization. The 2D iso-response profile is a contour plot that illustrates how the response variable changes as a function of two factors while keeping other factors constant. It consists of contour lines representing combinations of the two factors that yield the same response value. This visualization allows for easy identification of optimal regions and factor interactions. Moreover, the 3D iso-response profile extends this concept to three dimensions, offering a more comprehensive view of the relationship between factors and responses (Aziz & Aziz 2018). It is typically represented as a surface plot, where the x and y axes represent two factors, and the z-axis represents the response. The desirability profile is a method for simultaneous optimization of multiple responses. It involves transforming each response (Yi) into a dimensionless desirability function (di) that ranges from 0 to 1, where 0 represents a completely undesirable response and 1 represents the most desirable response. The overall desirability (D) is then calculated as the geometric mean of individual desirability following equation Eq. (2):

$$D = \sqrt[n]{d_1 \times d_2 \ldots \ldots \times d_n} \tag{2}$$

where n is the number of responses. This approach allows for the identification of factor levels that optimize multiple responses simultaneously, balancing potentially conflicting objectives (Haque et al. 2023). By maximizing the overall desirability, we can determine the optimal combination of factor levels for the entire system.

2.2.3 Micro-Analysis Equipment and Specifications

The XRD was performed using the D8 DISCOVER by BRUKER. The XRD system offers high precision with a minimum 2θ resolution of $0.01°$ and is capable of detecting phase differences down to the micrometer scale. The machine has been configured for a scan range of $5°$ to $70°$ 2θ with a step size of $0.02°$ 2θ to achieve detailed phase identification and quantification. The FTIR analysis was conducted using the VERTEX 70V by BRUKER. This advanced FTIR system provides high-resolution spectral data with wavenumber resolution down to 0.1 cm^{-1}, allowing precise characterization of molecular vibrations and functional groups. Analysis was performed over a wavenumber range of 4000 to 400 cm^{-1}. The SEM/EDX was performed using a JSM-IT 100 by JEOL. The SEM provides high-resolution imaging with a minimum resolution of 3 nm at 30 kV in high vacuum mode. The PSD was performed from SEM/EDX using ImageJ software, this provides high precision, flexibility, and advanced image processing tools.

2.2.4 Analysis of the Microstructural Properties of Pre-Geopolymer Powders

SEM and EDX analyses were employed to determine the morphology and chemical composition of the PGP as illustrated in Fig. 1. Owing to the high mechanical grinding potential of the raw materials (FA, NaOH, and Na$_2$SiO$_3$). The materials appear dense with few pores and cavities (P1, P3, P4, P5, and P8), and more pores and cavities (P2, P6, and P7) (Mucsi et al. 2015), as depicted in Fig. 1. The presence of an amorphous phase may be due to the high mechanical grounding condition of the raw materials and the variation in the Si/Al and Al/Na ratios of the geopolymer powder (Fig. 1) (Nada et al. 2019).

3 Results and Discussion

3.1 Compressive Strength and Density

The compressive strength and density results of 29 samples generated by the CCD design are presented in Table 4, the values are in the ranges of 11.22–32.41 MPa and 1.31–1.62 gr/cm^3 respectively, after curing for 28 days at ambient temperature. The highest compressive strength obtained was 32.41 MPa for the G6 sample prepared by grinding the

Fig. 1 a Micrographs SEM and EDX analysis of pre-geopolymer powders. (P1, P2, P3, P4) respectively. **b** Micrographs SEM and EDX analysis of pre-geopolymer powders. (P5, P6, P7, P8) respectively
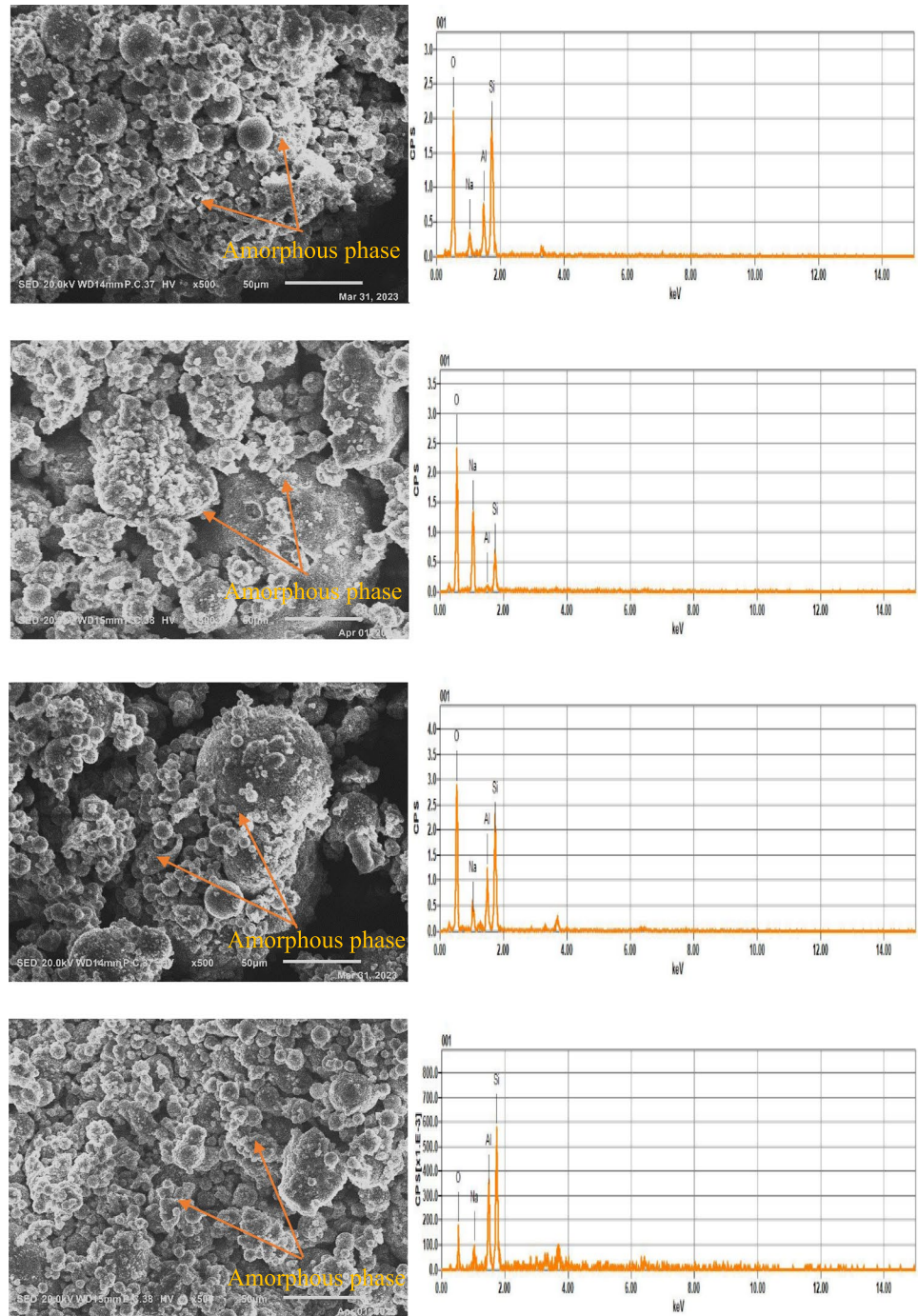

PGP at a rotational speed of 400 RPM for 5 min and then curing it at a temperature of 24 °C for 12 h. In contrast, the G26 sample exhibited a lower compressive strength at 11.22 MPa, and the PGP was prepared at a rotational speed of 350 RPM for 10 min and cured at 80 °C for 48 h. This can be explained by the higher curing temperature. The CCD approach was used to understand the influence of different parameters (grinding speed, grinding time, curing time, curing temperature, and NaOH concentration) on compressive strength and density.

3.2 Statistical Validation of the Polynomial of the Order 2 Model

The main effect of regression was statistically significant for both responses according to the analysis of variance results (Table 5) since the p-value of risk was less than 0.05 (< 0.0001). Moreover, the total squares resulting from the residuals are devised into a combination of the following variations: one is attributed to the lack of adjustment, and two is caused by pure error. The complementary

Fig. 1 (continued)
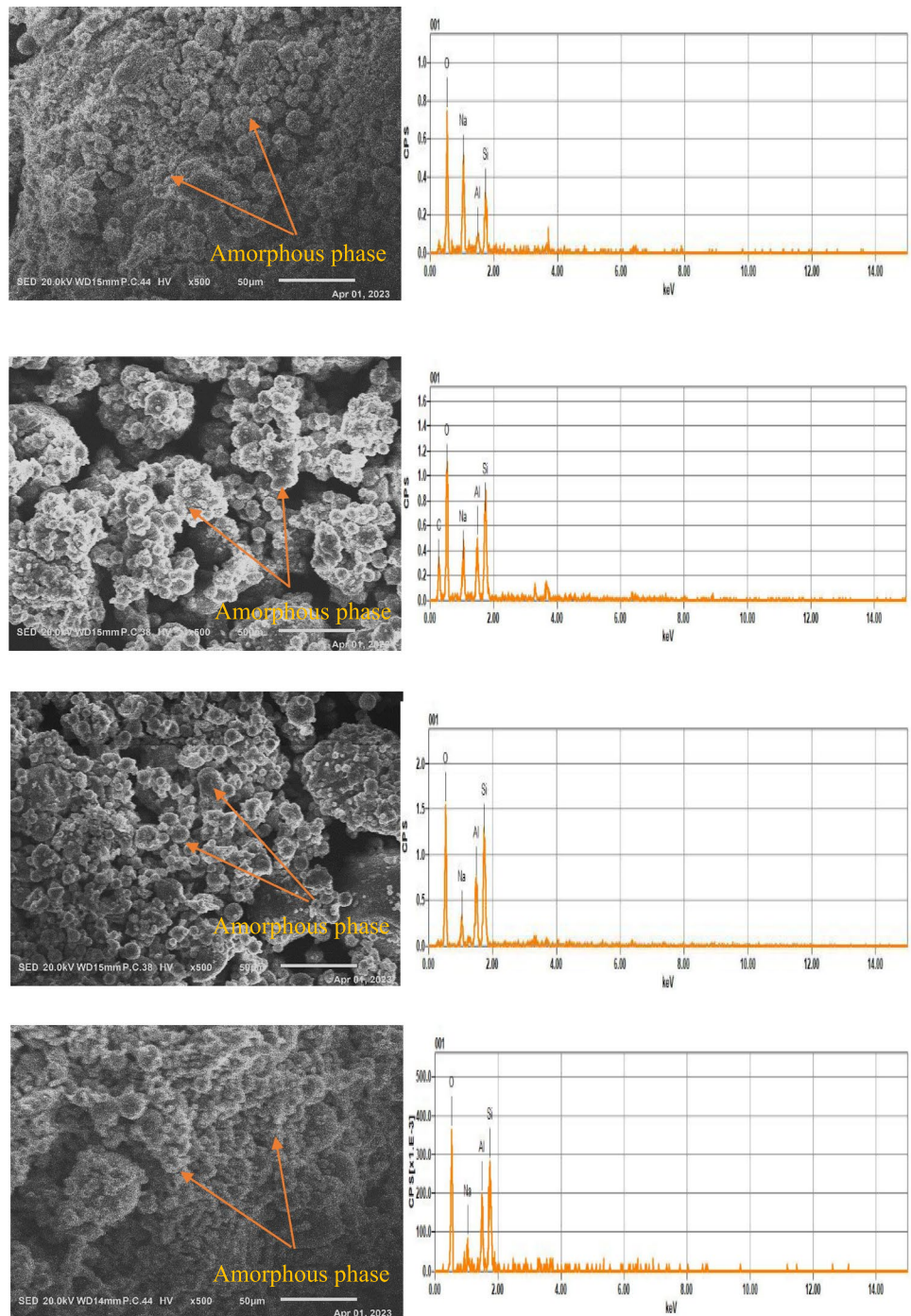
analysis of variance suggested that the model did not fit the data well since the risk value was greater than 0.05 (p-values = 0.11 and 0.10 for compressive strength and density, respectively) (Stella et al., 2022).

The graph illustrated in Fig. 2 reveals that the curve of values observed depending on the estimated values is linear. The model demonstrated strong predictive capabilities for both compressive strength and density. For compressive strength, the coefficient of determination (R^2) was 0.98, indicating that 98% of the variance in compressive strength was explained by the model. The Root Mean Squared Error (RMSE) was 1.33, signifying a relatively small average prediction error. For density, the R^2 was even higher at 0.99, suggesting an even stronger relationship between the model's predictions and the actual density values. The RMSE for density was significantly lower

Table 4 Experimental matrix generated by the CCD design and the relative responses of materials

Experience N°	NaOH (M)	Grinding speed (RPM)	Grinding time (min)	Curing temperature (°C)	Curing time (min)	Compressive strength (MPa)	Density (gr/cm^3)
1	10	300	5	24	24	22.51	1.54
2	10	300	5	80	12	24.86	1.43
3	16	300	5	80	24	23.27	1.48
4	16	300	5	24	12	23.56	1.47
5	10	400	5	80	24	28.56	1.39
6	10	400	5	24	12	32.41	1.62
7	16	400	5	24	24	30.95	1.59
8	16	400	5	80	12	28.84	1.48
9	10	300	15	80	24	30.45	1.61
10	10	300	15	24	12	25.75	1.47
11	16	300	15	24	24	22.84	1.36
12	16	300	15	80	12	29.67	1.31
13	10	400	15	24	24	16.82	1.45
14	10	400	15	80	12	13.22	1.43
15	16	400	15	80	24	14.08	1.32
16	16	400	15	24	12	18.69	1.32
17	13	350	5	52	48	23.59	1.59
18	13	350	15	52	48	24.87	1.50
19	13	300	10	52	48	21.04	1.49
20	13	400	10	52	48	14.06	1.51
21	10	350	10	52	48	19.74	1.62
22	16	350	10	52	48	19.52	1.52
23	13	350	10	52	24	17.86	1.57
24	13	350	10	52	12	18.01	1.52
25	13	350	10	24	48	13.20	1.56
26	13	350	10	80	48	11.22	1.57
27	13	350	10	52	48	13.86	1.58
28	13	350	10	52	48	13.94	1.59
29	13	350	10	52	48	14.79	1.58

Table 5 Analysis of variance of the fitted model

Response	Compressive strength (MPa)				Density (gr/cm^3)			
Source of variance	DF	Sum of squares	Mean square	F ratio	p-value	Sum of squares	Mean square	F ratio	p-value
Regression	20	1072.01	53.6	30.01	<0.0001	0.23954	0.01198	49.6	<0.0001
Residual	8	14.29	1.79			0.00193	0.00024		
Lack of fit	6	13.76	2.29	8.63	0.11	0.00187	0.00031	9.33	0.10
Pure error	2	0.53	027			0.00007	0.00003		
Total	28	1086.29				0.24147			
Square			0.98					0.99	

at 0.015, indicating highly accurate predictions with minimal average error. These results suggest that the model effectively captures the key factors influencing both compressive strength and density, providing reliable predictions for these critical material properties.

3.3 Factor Effects and Coefficient Estimations

Table 6 shows the statistical values of the t-student test and the corresponding observed probabilities, illustrating the impact of all the factors examined.
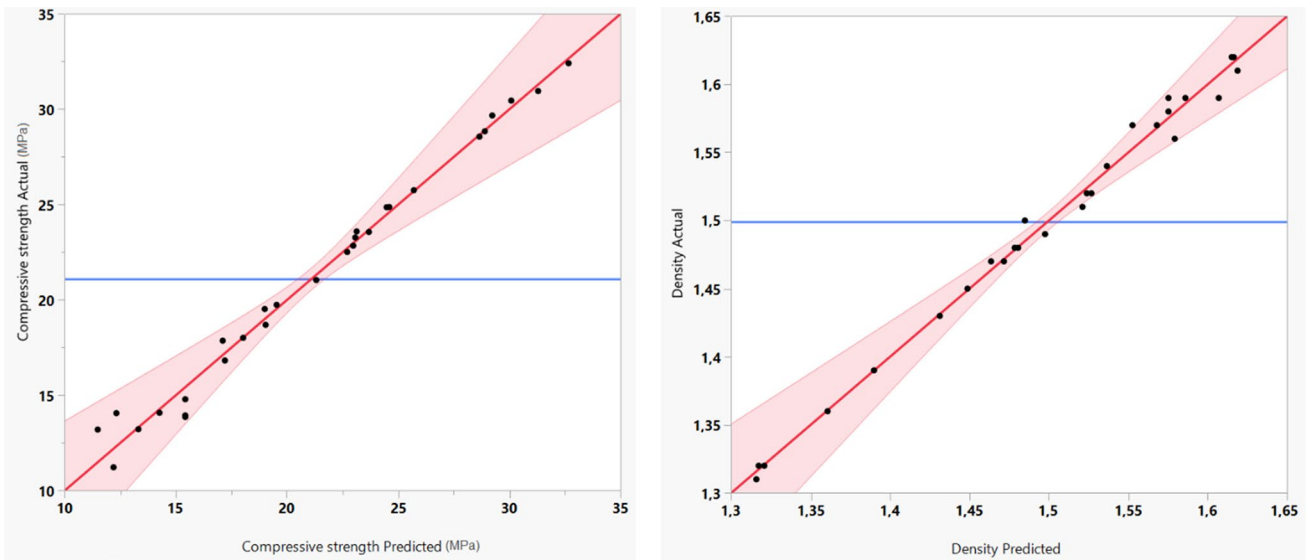
Fig. 2 Relationship between Actual and Predicted value of the responses compressive strength (**A**) and density (**B**). The red curve represents the regression line, indicating the trend between predicted and actual responses. The pink shaded area represents the 95% confidence interval around the regression line. The blue horizontal line shows the mean of all actual response values

Table 6 Impact of the model coefficient response relating to factors

Term	Coefficient	Compressive strength (MPa)		Density (gr/cm³)	
		Estimate	Prob >|t|	Estimate	Prob >|t|
Intercept	b_0	15.23	<0.0001*	1.57	<0.0001*
Grinding duration	b_1	1.02	0.073	−0.05	<0.0001*
Grinding speed	b_2	−5.14	<0.0001*	0.00	0.639
NaOH concentration	b_3	−0.25	0.486	−0.05	<0.0001*
Curing time	b_4	0.30	0.412	−0.03	0.0002*
Curing temperature	b_5	−1.21	0.019*	−0.01	0.025*
Grinding duration*Grinding speed	b_{12}	−7.94	<0.0001*	−0.01	0.281
Grinding duration*NaOH concentration	b_{13}	−0.07	0.846	−0.05	<0.0001*
Grinding speed*NaOH concentration	b_{23}	0.47	0.317	0.02	0.003*
Grinding duration*Curing time	b_{14}	−0.04	0.911	−0.02	0.001*
Grinding speed*Curing time	b_{24}	−0.15	0.748	0.03	0.0002*
NaOH concentration*Curing time	b_{34}	1.29	0.006*	0.00	0.891
Grinding duration*Curing temperature	b_{15}	0.72	0.02*	0.03	<0.0001*
Grinding speed*Curing temperature	b_{25}	−1.60	0.001*	−0.02	0.0004*
NaOH concentration*Curing temperature	b_{35}	0.04	0.890	0.00	0.334
Curing time*Curing temperature	b_{45}	−0.40	0.151	−0.01	0.029*
Grinding duration*Grinding duration	b_{11}	8.44	<0.0001*	−0.03	0.017*
Grinding speed*Grinding speed	b_{22}	1.40	0.123	−0.07	0.0001*
NaOH concentration*NaOH concentration	b_{33}	3.84	0.002*	0.00	0.665
Curing time*Curing time	b_{44}	2.14	0.033*	−0.03	0.017*
Curing temperature*Curing temperature	b_{55}	−1.83	0.003*	0.00	0.364

According to the results, the statistical coefficients supposed to be significant for the compressive strength response are the constant values of b_0, the straight-line terms (b_1, b_3, b_4, and b_5), the quadratic terms (b_{11}, b_{22}, and b_{44}), and the interactive terms (b_{13}, b_{23}, b_{14}, b_{24}, b_{15}, b_{25}, and b_{45}). All these factors had *p*-values less than 0.05 are indicated in red as shown in

Table 6. Consequently, the mathematical model for compressive strength is as follows Eq. (3):

$$
\begin{aligned}
Y_{Compressivestrength} =& 15.23 - 5.14X_2 - 1.21X_5 + 8.44X_1X_1 \\
&+ 3.84X_3X_3 + 2.14X_4X_4 \\
&- 1.83X_5X_5 - 7.94X_1X_2 + 1.29X_3X_4 \\
&+ 0.72X_1X_5 \neg 1.60X_2X_5 + \varepsilon
\end{aligned}
\tag{3}
$$

The compressive strength response equation reveals significant interactions between several pairs of variables, indicating that optimizing strength requires considering their combined effects. A negative interaction between grinding duration (X_1) and speed (X_2) suggests that increasing both factors together might lead to a smaller increase in strength compared to increasing either factor alone. Conversely, a positive interaction exists between grinding duration (X_1) and curing temperature (X_5), indicating that increasing both variables simultaneously might result in a greater increase in strength. A similar positive interaction is observed between NaOH concentration (X_3) and curing time (X_4). Finally, a negative interaction exists between grinding speed (X_2) and curing temperature (X_5), suggesting that increasing both factors might lead to a smaller increase in strength compared to increasing either factor alone.

According to the values in Table 6, the statistical coefficients for the density response are the constant b_0, the straight-line terms (b_2 and b_5), the quadratic terms (b_{11}, b_{33}, b_{44}, and b_{55}), and the interactive terms (b_{12}, b_{34}, b_{15}, and b_{25}). All these factors had p-values less than 0.05. Therefore, the mathematical model representing the density Eq. (4) is concluded to be:

$$
\begin{aligned}
Y_{Density} =& 1.57 - 0.05X_1 - 0.03X_3 - 0.01X_5 - 0.03X_1X_1 \\
&- 0.07X_2X_2 - 0.05X_1X_3 + 0.02X_2X_3 \\
&- 0.02X_1X_4 + 0.03X_2X_4 + 0.03X_1X_5 - 0.01X_4X_5 + \varepsilon
\end{aligned}
\tag{4}
$$

The density response equation highlights several significant interactions between design variables, indicating that optimizing density requires considering their combined effects. A negative interaction exists between grinding duration (X_1) and NaOH concentration (X_3), suggesting that increasing both factors might lead to a smaller increase in density compared to increasing either factor alone. Conversely, a positive interaction is observed between grinding speed (X_2) and NaOH concentration (X_3), indicating that increasing both variables simultaneously might result in a greater increase in density. Similar positive interactions are found between grinding speed (X_2) and curing time (X_4) as well as between grinding duration (X_1) and curing temperature (X_5). Finally, a negative interaction exists between curing time (X_4) and curing temperature (X_5), suggesting that increasing both factors might lead to a smaller increase in density compared to increasing either factor

alone. These interactions emphasize the need to carefully balance these variables to achieve optimal density.

3.4 Optimization of Parameters

3.4.1 Compressive Strength Response

A primary analysis of the data showed that achieving the highest compressive strength response is contingent upon the highest compressive strength obtained with 32.41 MPa, for the G6 sample prepared by grinding the PGP at a rotational speed of 400 RPM for 5 min and then curing it at a temperature of 24 °C for 12 h and finally adjusting the curing temperature to an optimum value. Since the representation is only in 2D, two of the five factors were chosen to represent the factors to their optimal values. In this case, the grinding duration and curing temperature represent the compressive strength response, at the same fixing three factors (grinding speed, NaOH concentration, and curing time) to their minimal level, which represents their optimal settings as shown in Fig. 3.

3.4.1.1 (a) Profile of the *Iso*-Response Compressive Strength In 2D and 3D With the aid of the iso-response profile (Fig. 3), different solutions have been proposed for operating conditions.

An analysis based on the 2D and 3D iso-response plots indicates that a compressive strength of approximately 45 MPa can be achieved by carefully controlling specific parameters. Grinding the material for approximately 15 min is crucial, while the curing temperature needs to be between 46 and 80 °C. The grinding duration might be flexible. Additionally, three other factors, grinding speed (300 RPM), NaOH concentration (10 M), and curing time (24 h), are assumed to be optimal for achieving an optimal response of 45 MPa. Comparable to ordinary Portland cement, the typical compressive strength of ordinary Portland cement concrete, generally ranges from 20 to 40 MPa for standard mixes used in residential and commercial construction(Yang et al. 2023).

3.4.1.2 (b) Desirability Profile of the Compressive Strength By utilizing a desirability function, researchers were able to fine-tune the optimization process to achieve a specific compressive strength with high precision. Figure 4 reveals that a desirable outcome of 47.12 MPa can be reached with a near-perfect desirability of 99% under the following precise conditions: 300 RPM grinding speed, 15 min of grinding time, 24 h of curing time, a curing temperature of 68 °C, and 10 M NaOH concentration.
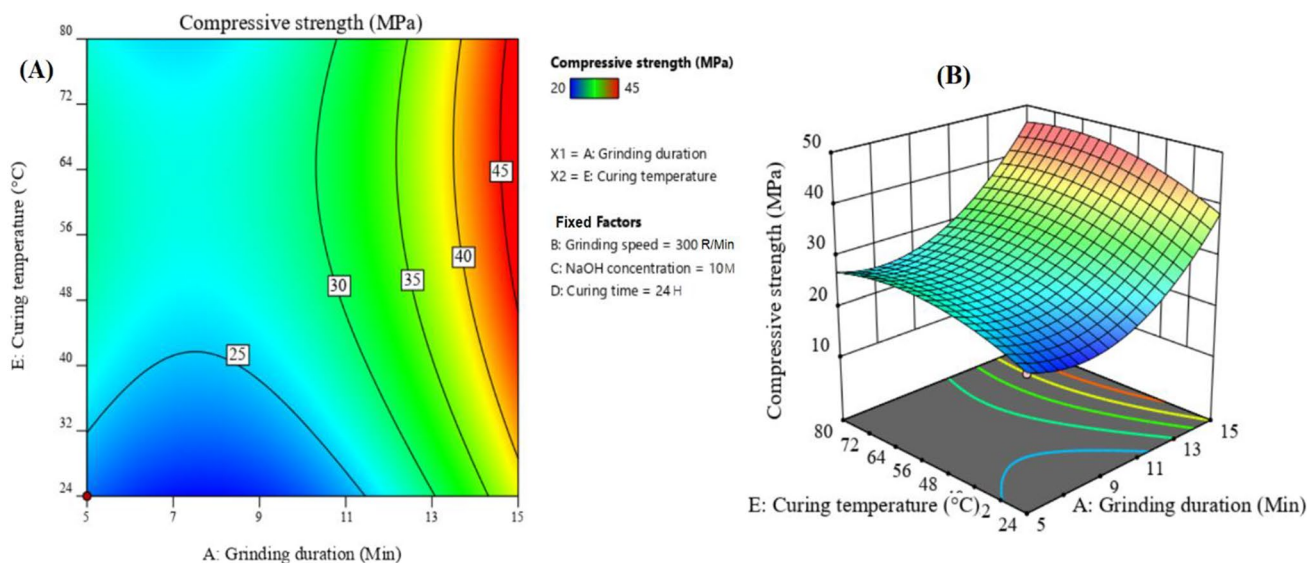
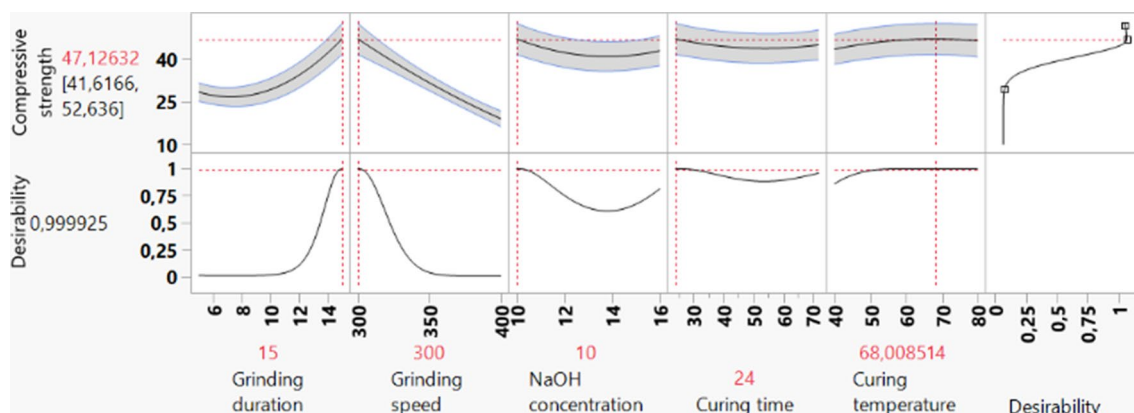**Fig. 3** The contour plots of the compressive strength response: **a** 2D; **b** 3D

Fig. 4 Desirability profile of the optimal conditions for the compressive strength response

3.4.2 Density Response

A primary analysis of the data showed that maximizing the density response depended on maximizing grinding duration and curing temperature, minimizing two factors curing time, and NaOH concentration, and finally adjusting the grinding speed to an optimum value. In this case, grinding duration and grinding speed were selected to represent the density response, at the same fixing three factors (curing temperature, NaOH concentration, and curing time) to their minimal level, which represents their optimal settings as shown in Fig. 5.

3.4.2.1 (a) Profile *Iso*-Response Density in 2D and 3D With the aid of the iso-response profile (Fig. 5), different solutions have been proposed for operating conditions.

Both the 2D/3D contour plots and the desirability function analysis point toward achieving a density of approximately 1.64 gr/cm^3. The contour plots (Fig. 5) suggest a grinding speed range of 306–332 RPM at a fixed grinding time (15 min), curing time (24 h), curing temperature (80 °C), and NaOH concentration (10 M).

3.4.2.2 (b) Desirability Profile of Density However, for a more precise approach, the desirability function (Fig. 6) recommends specific conditions to reach this density with
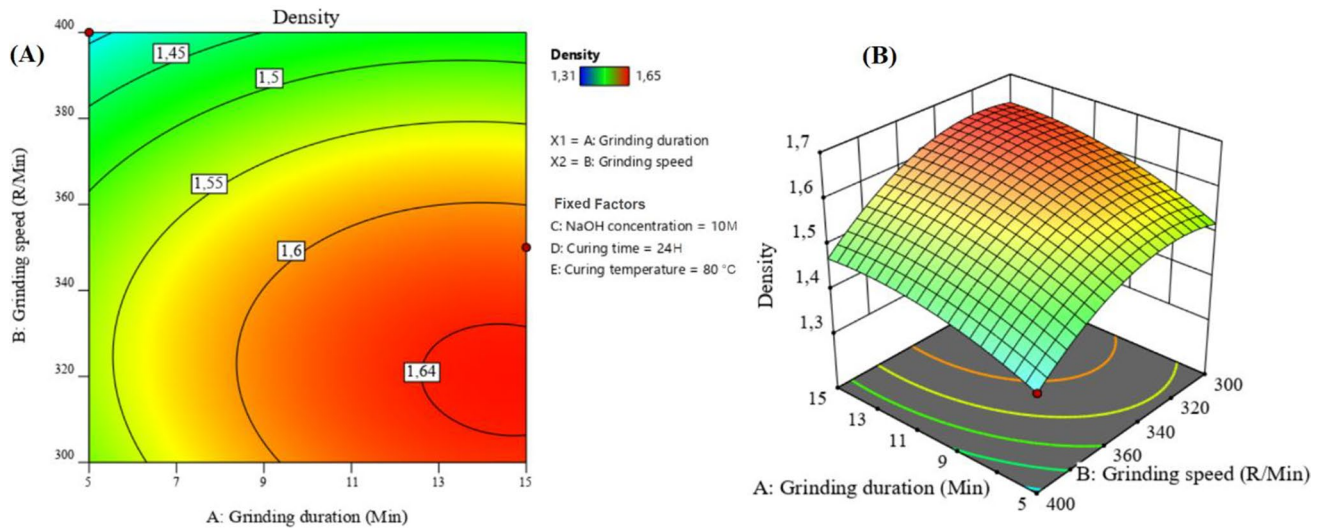
Fig. 5 The contour plots of the density response: **a** 2D; **b** 3D
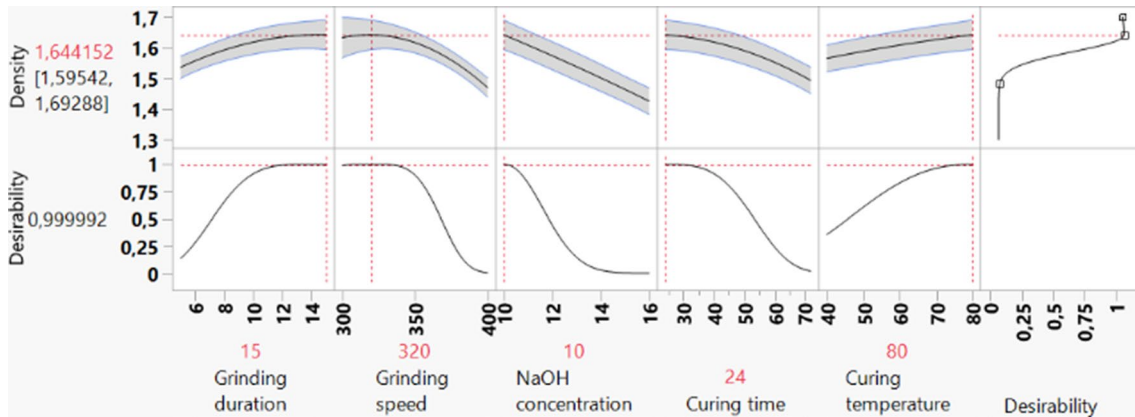
Fig. 6 Desirability profile of the optimal conditions for the density response

near-perfect accuracy (99% desirability): 320 RPM grinding speed, 15 min grinding time, 24 h curing time, 80 °C curing temperature, and 10 M NaOH concentration.

3.4.3 Simultaneous Optimization of Both Responses

From the individual optimization studies for each response, it is evident that the optimal conditions for both responses exhibit nearly identical correlations, as depicted in Figs. 4 and 6. This finding suggested the possibility of identifying a single set of parameters that optimizes both responses simultaneously.

As illustrated in Fig. 7, achieving the optimal balance between compressive strength and density is possible. By

following a specific set of parameters, it is possible to obtain a desirable outcome for both responses with a near-perfect level of precision (approximately 99% desirability).

The optimal parameters for the simultaneous optimization of compressive strength and density were 300 RPM, 15 min, 24 h, 80 °C, and 10 M, grinding speed, grinding time, curing time, curing temperature, and NaOH concentration, respectively.

The similar optimization tendencies of the two responses suggest a significant correlation between them. Indeed, A strong positive correlation ($r = 0.92$, $p < 0.0001$) was observed between compressive strength and density, indicating a significant association between these two properties. This finding suggests that as density increases, compressive strength also tends to increase
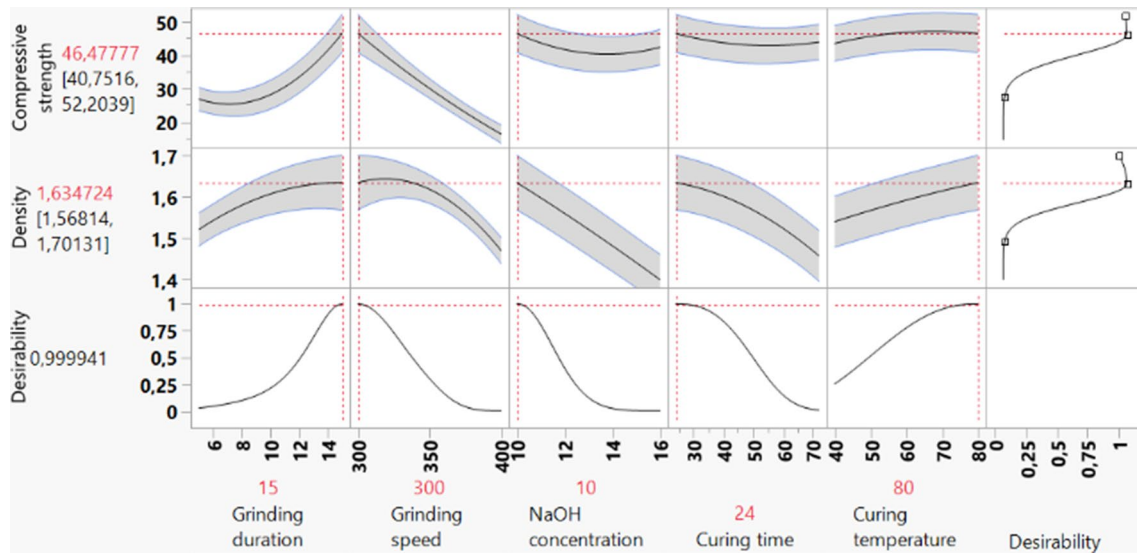
Fig. 7 Desirability profile of the optimal conditions for both compressive strength and density

proportionally. This relationship highlights the interconnected nature of these material properties and has important implications for understanding the overall performance and behavior of the material.

3.5 Comparative Studies on the Application of CCD in Optimization

In this section, the optimization results obtained in this study will be compared with those of previous research, despite the absence of studies combining both experimental design in optimization and the adoption of the mechanosynthesis method simultaneously.

While X. Shi et al. focused on optimizing the composition and curing conditions of geopolymers using the response surface method to predict the influence of varying parameters on key properties, our study emphasizes the application of the central composite design (CCD) (Shi et al. 2022). The CCD design efficiently estimates the main effects and minimizes the number of experiments compared to other factorial designs, providing a robust framework for optimization.

3.6 Analysis of the Structural and Microstructural Properties of Geopolymers

The fly ash geopolymer samples, distinguished by their high mechanical performance (G6, G9, and G12), and low mechanical performance (G26) were characterized using XRD, FT-IR, and SEM–EDX analyses.
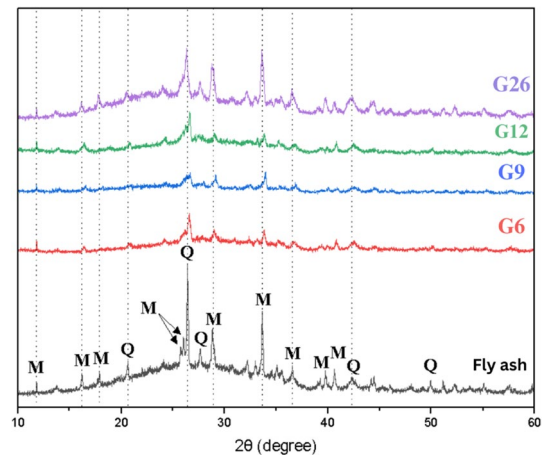

Fig. 8 XRD analysis of the raw fly ash and geopolymer prepared according to the mechanosynthesis process (G6, G9, G12, and G26)

3.6.1 X-ray Diffraction Analysis

XRD patterns of the fly ash-based geopolymer, as depicted in Fig. 8, highlight a detailed comparison between the raw fly ash and geopolymer samples prepared through the mechanosynthesis process (G6, G9, G12, and G26). In the XRD patterns of the raw fly ash, various peaks corresponding to crystalline phases including quartz and, mullite, were identified (Kosor et al. 2016; Murmu et al. 2020; Zhang et al. 2023a, b).

In contrast, the geopolymer samples exhibited various modifications, such as alterations in peak intensity, the emergence of new peaks, and the disappearance of other peaks. For example, amorphous phases (Liu et al. 2016; Ndlovu et al. 2017). The amorphous phase is typically denser and more homogeneous compared to crystalline phases in geopolymer materials typically formed from the aluminosilicate gel. The optimized processing conditions identified in our study led to the production of a geopolymer with a high degree of amorphousness. This amorphous phase is responsible for the material's cohesion and significantly contributes to its compressive strength (Zhang et al. 2023a, b). These observations provide valuable insights into the structural changes and transformations that occur during the polymerization process, shedding light on the material's composition

and characteristics (Payakaniti et al. 2020). The XRD patterns of the geopolymer samples produced by mechanosynthesis (G6, G9, G12, and G26) clearly show the formation of an amorphous phase. The formation of the amorphous phase was confirmed by the presence of a wide band at 2θ values between 15 and 40°. This finding agrees with the findings of Sanalkumar et al. (Ambikakumari Sanalkumar et al. 2019). This observation highlights the successful incorporation of amorphous phases during geopolymerization underscoring the transformative impact of the mechanosynthesis process and the temperature on the material composition (Han et al. 2020; Mahfoud et al. 2023; Zerzouri et al. 2022).

The observed decreases in the peak intensities of quartz, and mullite in the XRD patterns of the fly ash-based geopolymer, particularly in the high-performance samples (G6, G9, and G12) compared to those of the low-performance geopolymer G26 can be attributed to the inherent nature of the material. This phenomenon is a consequence of the material's high predisposition to form stable crystalline phases. Upon grinding and curing under diverse conditions, the initial comparison between raw fly ash and the geopolymer samples indicated a decrease in peak intensities (Nath & Kumar 2020). This reduction is associated with the type and arrangement of atoms within the crystal structure. Notably, high-performance geopolymers (G6, G9, and G12) exhibit lower peak intensities than low-performance geopolymer G26 (Jiang et al. 2020; Luo et al. 2022). This suggests that the latter lacks sufficient energy to arrange atoms effectively in the crystal structure, contributing to its comparatively lower mechanical strength (Shilar et al. 2022; Ziegler et al. 2016).

3.6.2 FT-IR Analysis

The resulting spectra of both the Raw Fly Ash (Raw FA) and the geopolymer samples prepared through the

Fig. 9 FT-IR spectra of the raw FA and geopolymer prepared according to the mechanosynthesis process (G6, G9, G12, and G26)

Table 7 The most important IR bands and their assignments for the raw FA and the synthesized geopolymer materials

Wavenumbers (cm^{-1})	Assignments	References
400–562	O–Si–O bending modes	(Aouan et al. 2021)
812–994	Si–O stretching vibration	(Aouan et al. 2021)
900–1000	Vibrations of Si–O	(Aouan et al. 2022)
900–1100	Asymmetrical stretching vibration Si–O–Al and Si–O–Si	(Aouan et al. 2022)
1460	O–C–O stretching vibration of the carbonate phase	(Aouan et al. 2023a, b)
1630–1670	O–H bending vibration	(Aouan et al. 2023a, b)
2300–2500	Vibrational deformation of H–O–H groups	(Aouan, Alehyen, Fadil, El Alouani, Saufi, El Herradi, et al., 2023)
3300–3500	Stretching vibrations of the –OH and H–O–H bonds	(Aouan, Alehyen, Fadil, El Alouani, Saufi, El Herradi, et al., 2023)

mechanosynthesis process (G6, G9, G12, and G26) shown in Fig. 9, and all assignments of the observed infrared bands are presented in Table 7. The IR spectra exhibit distinct groups of bands. This provides a comprehensive overview of all the band assignments, as described in Fig. 9.

In contrast to the infrared spectra of raw FA, all the synthesized geopolymers exhibited a distinct band at 418 cm^{-1}, corresponding to O–Si–O bending modes (Bornhauser & Calzaferri 1996; Chen et al. 2022). Additionally, the peak within the 560 cm^{-1} range is attributed to the asymmetrical stretching vibrations of Si–O–Al (Mozgawa et al. 2014; Yan et al. 2012). These observations suggest alterations in molecular structure and bonding configuration during the geopolymerization process.

The Si–O stretching vibration is notably observed at 845 cm^{-1} (Tchakouté et al. 2017) in the infrared spectra. Furthermore, a smaller band is associated with the vibration of Si–O within the range of 900–1000 cm^{-1}. The intense banding between 900 and 1100 cm^{-1} is attributed to the asymmetrical stretching vibrations of Si–O–Al and Si–O–Si, indicating the formation of amorphous aluminosilicate (Handke 1986; Rathee et al. 2023; Šontevska et al. 2007). These specific bands in the infrared spectra provide valuable insights into the structural changes and chemical compositions of geopolymers, particularly highlighting the development of amorphous aluminosilicate during geopolymerization.

The peak observed at 1460 cm^{-1} could be linked to the O–C–O stretching vibration of the carbonate phase. However, these bands present challenges in clearly assigning vibrational modes within the same range as the mineral matrix. It is plausible that these features result from the reaction between the alkaline activator and atmospheric CO$_2$ (Phair & Van Deventer 2002; Samouh et al. 2023). This observation underscores the importance of considering environmental factors and secondary reactions, contributing to a more nuanced understanding of the material's composition and the effects of external conditions on its vibrational spectra.

The presence of bands in the region at 1671 cm^{-1} suggested that they corresponded to the O–H bending vibration of water molecules similar to the small band between 3300 and 3500 cm^{-1}, which is attributed to the stretching vibrations of the –OH and H–O–H bonds (Puertas et al. 2006; Yan et al. 2012). Additionally, the lower frequency band observed at 2335 cm^{-1} corresponds to the H–O–H group bonds of free H$_2$O particles (Aouan et al. 2023a, b). These observations in the infrared spectra indicate the involvement of water molecules and the presence of different types of bonds in the geopolymer structure, providing valuable information about the hydration and composition of the material. It is crucial to emphasize that the deviation of the band fly ash should be located normally at 1070 or 1100 cm^{-1} to 980 cm^{-1} for the four geopolymers (G6, G9, G12, and

G26), which signifies a noteworthy shift, serving as a clear indication of sodium aluminosilicate hydrate (NASH) gel formation during the geopolymerization process (Khan et al. 2020).

3.6.3 SEM/EDS Analysis

Figure 10, which displays the SEM and EDS results of geopolymers prepared through mechanosynthesis (G6, G9, G12, and G26), offers a comprehensive view of the surface and morphology of the material. SEM images reveal the topography, microstructure, surface finish, and surface characteristics of the material (Rahimzadeh et al. 2024). On the other hand, EDS allows for the spatial distribution analysis of each element present in the sample (Epstein & Stolper 1992).

The initial comparison involved SEM images of geopolymers derived from fly ash (FA) through the mechanosynthesis process (Fig. 10), contrasting high-performance materials (G6, G9, and G12) with low-performance materials (G26). This reveals notable distinctions in the texture and size of the particles, which are primarily characterized by their spherical and granular nature (Grabias-Blicharz et al. 2022). Samples G6, G9, and G12 exhibit a dense and uniform structure characterized by small particles ranging from 1.2 to 17.20 μm in size. This characteristic is indicative of high compressive strength, as detailed in Table 2. In contrast, G26 displays a lower resistance performance attributable to its heterogeneous and porous structure, featuring particles with diameters spanning from 3.4 to 27.412 μm (Wang et al. 2011). The geopolymer G6, derived from the grinding of powder P1 at 400 R/min for 5 min, exhibited a significant decrease in particle size. The particles are predominantly spherical, varying in size, and are referred to as microspheres. These microspheres can be either compact or hollow. Similar processes involving grinding at 300 R/min for 15 min were used to prepare geopolymers G9 and G12 from P3 powder. On the other hand, the geopolymer G26, which was also derived from powder P3 but ground at 350 R/min for 10 min, did not achieve a sufficient reduction in particle size comparable to that of other high-performance geopolymers (Rodrigue Kaze et al. 2021). The resulting cavities between particles in these geopolymers play a crucial role in influencing the mechanical strength and density (Cao et al. 2018).

The EDS analysis depicted in Fig. 10 reveals that the major components of all geopolymer systems include silicon (Si), aluminum (Al), sodium (Na), and oxygen (O). These elements are of utmost importance for the mechanical properties of geopolymer materials and are essential constituents of the N-A-S–H (sodium–alumino–silicate hydrate) geopolymer gel. Additionally, there are trace amounts of other elements such as calcium (Ca), and magnesium (Mg). However, these elements are present in small proportions
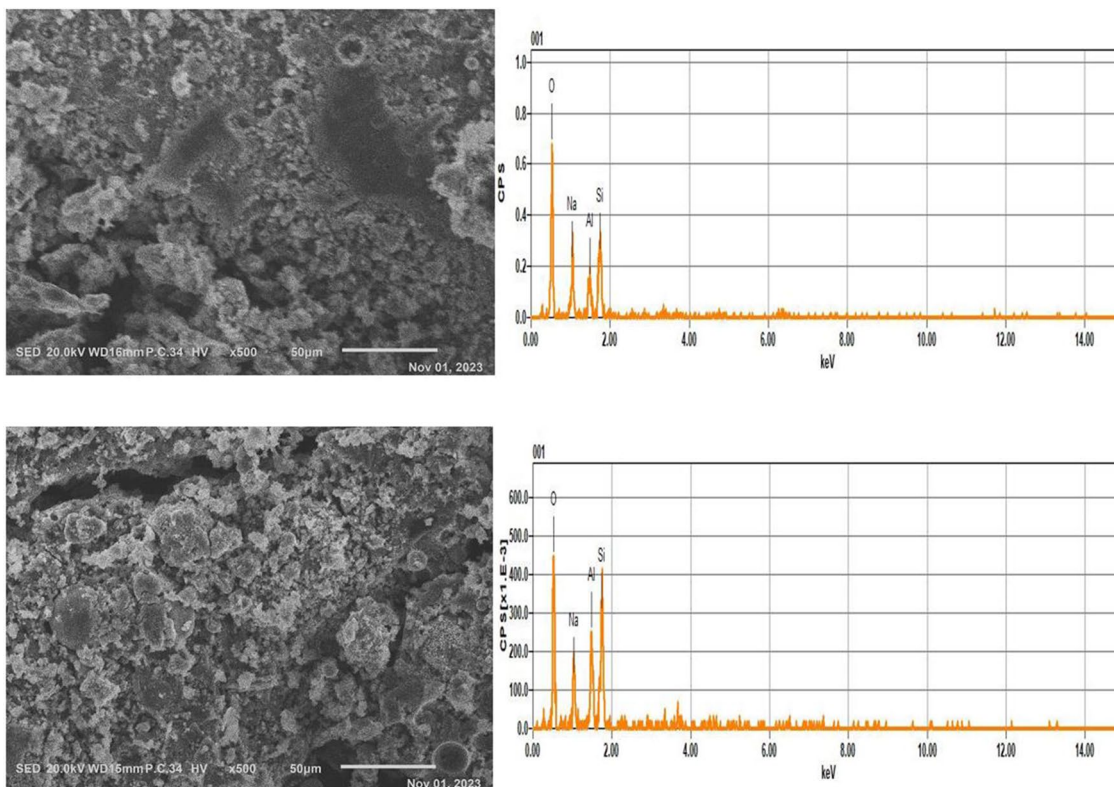
Fig. 10 a SEM/EDX images of geopolymer prepared according to the mechanosynthesis process (G6, and G9) respectively. **b** SEM/EDX images of geopolymer prepared according to the mechanosynthesis process (G12, and G26) respectively

and are stated to have no notable impact on the mechanical properties of geopolymer materials (Carrilero et al. 2002; Ryu et al. 2013).

3.6.4 PSD Analysis

The resulting particle size distribution (PSD) curve of both the FA and the geopolymer samples (G6, G9, G12, and G26) derived from SEM/EDX analysis is shown in Fig. 11, this provides valuable insights into the microstructure of Fly ash and geopolymers. On the other hand, PSD can enhance the understanding of material properties and help to correlate particle size with mechanical properties.

The average diameter of the particles measured calculated is 7.197 μm, 7.475 μm, 8.081 μm, 8.567 μm, and 9.120 μm for FA, G6, G9, G12, and G26 respectively. The initial comparison of the average diameter of high-performance materials (G6, G9, and G12) with low-performance materials (G26) shows that particle size affects mechanical properties (Bhina et al. 2024), the particle size of high-performance appears smaller than low-performance geopolymer G26. The smaller particles generally signify a more uniform and dense geopolymer, this

may contribute to enhancing the compressive strength of geopolymers (Pan et al. 2024).

The cumulative percent values for the fly ash curve show a high increase at smaller particle sizes and reach 100% gradually at around 17 μm, indicating a finer distribution (Wang et al. 2024). In contrast, the curve of the geopolymer samples indicates that their particles reach high cumulative percentages at higher particle sizes, reflecting larger and more varied particle sizes (Yong-Jie et al. 2024).

4 Conclusions

In this study, a mathematical statistical approach based on the CCD methodology was adopted to optimize the mechanical properties of a fly ash-based geopolymer paste. In addition, a novel method for improving the reactivity of precursors, namely mechanosynthesis, was explored for the preparation of PGPs. Through the application of the central composite methodology, several critical parameters for fly ash-based geopolymer production were successfully optimized in this study. These parameters include grinding speed and duration, curing time and temperature, and NaOH
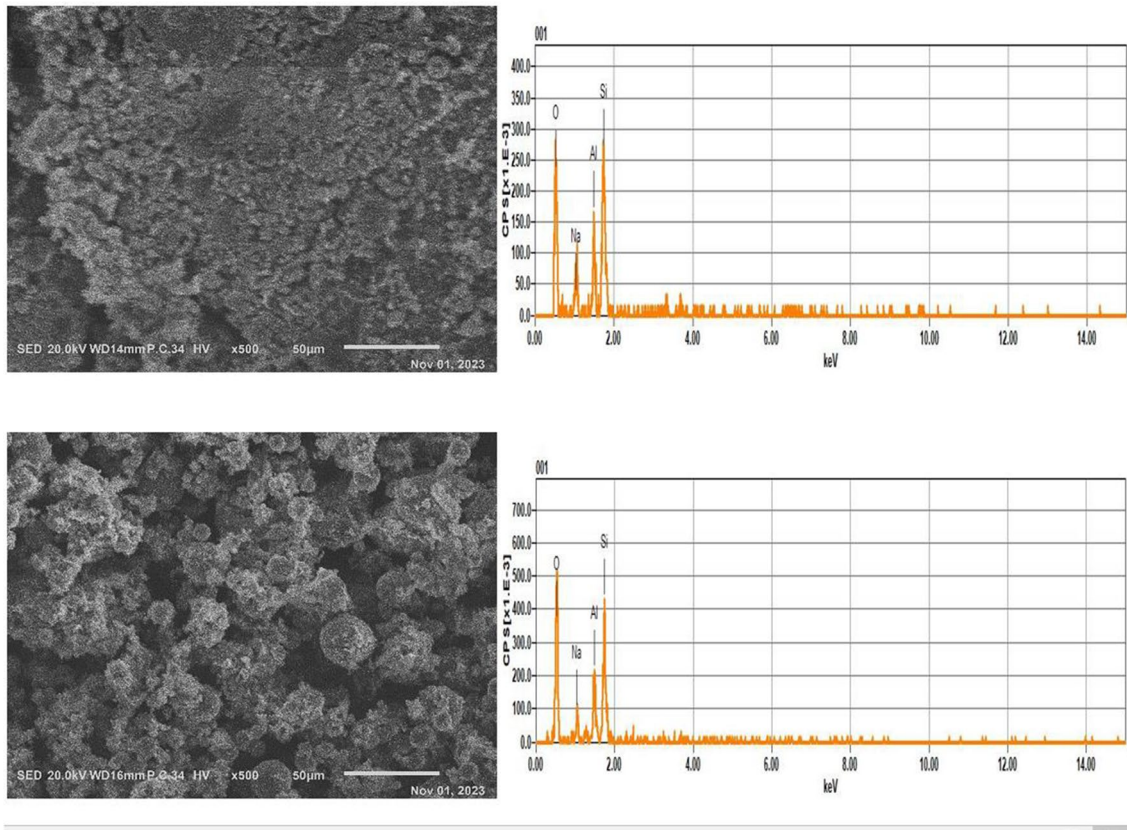
Fig. 10 (continued)

concentration. The optimized conditions resulted in remarkable mechanical properties, with a compressive strength of 46.47 MPa and a density of 1.64 gr/cm^3 for the geopolymer samples. This achievement underscores the effectiveness of the optimization process in enhancing the mechanical performance of the geopolymer. The identified optimal operating conditions for producing high-performance geopolymer paste include a grinding speed of 300 rpm, a grinding time of 15 min, a curing time of 24 h, a curing temperature of 80 °C, and a 10 M NaOH concentration. Various characterization techniques, including X-ray diffraction (XRD), Fourier-transform infrared spectroscopy (FTIR), scanning electron microscopy (SEM), and energy-dispersive X-ray spectroscopy (EDX), The X-ray Fluorescence (XRF) technique, were employed to investigate the structural and morphological characteristics of the raw materials and the synthesized geopolymer samples. The analyses revealed significant insights into the composition and structure of the geopolymers. Notably, XRD analysis revealed primarily bands, while FTIR analysis indicated that bond intensities are conducive to the formation of amorphous aluminosilicate. SEM/EDX observations highlighted differences in particle nature and size between high-performance and low-performance geopolymers. The observed differences in

particle size, particularly for nanocrystals, were found to correlate with variations in compressive strength. This finding underscores the importance of particle size in determining the mechanical properties of geopolymers. While this study has made significant strides in optimizing geopolymer production parameters. Future investigations could further
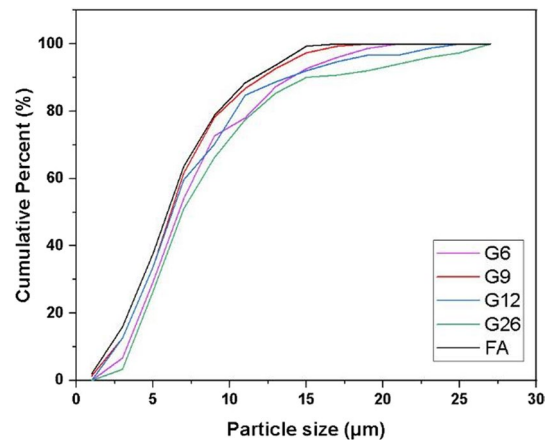

Fig. 11 PSD Curve of fly ash and geopolymer samples (G6, G9, G12, and G26) from SEM/EDX

Springer

investigate the influence of additional factors and refine the optimization process to achieve even better performance. Investigate the use of different alternative Precursors such as slag, red mud, or rice husk ash or natural pozzolans such as volcanic ash or pumice. The exploration of different alkaline activators such as the combination of KOH and NaOH, Studies the effect of different parameters that might improve the performance of geopolymers such as granulometry or Shrinkage, Cracking Control, and adjusting mix design as BBD or Taguchi. In conclusion, the findings of this study not only contribute to the optimization of parameters for enhancing mechanical performance but also provide valuable insights into the advancement of geopolymer technology and its abilities. The optimized geopolymer paste exhibited promising characteristics, laying a foundation for continued exploration and application in various engineering and construction applications.

Author Contributions Y.E. wrote the main manuscript text. Y.E. and S.A. and M.F. conceptualized the study and designed the research. Y.E. and M.F. and A.L. conducted the experiments and collected the data. M.F. and Y.E. performed the statistical analysis. Y.E. and M.T. and A.L. contributed to data interpretation. All authors read and approved the final version of the manuscript.

Data Availability No datasets were generated or analysed during the current study.

Declarations

Conflict of interest The authors declare that they have no known competing financial interests or personal relationships that could have appeared to influence the work reported in this paper. The authors declare no competing interests.

References

Addis LB, Sendekie ZB, Habtu NG, de Ligny D, Roether JA, Boccaccini AR (2023) Optimization of process parameters for the synthesis of class F fly ash-based geopolymer binders. J Clean Product. https://doi.org/10.1016/j.jclepro.2023.137849

Ahmad I, Basu D (2024) Experimental study and response surface methodology optimization of electro-fenton process reactive orange 16 dye treatment. Iran J Sci Technol Trans Civil Eng 48(3):1715–1729. https://doi.org/10.1007/s40996-024-01442-5

Ahmed HU, Mohammed AS, Faraj RH, Abdalla AA, Qaidi SMA, Sor NH, Mohammed AA (2023) Innovative modeling techniques including MEP, ANN and FQ to forecast the compressive strength of geopolymer concrete modified with nanoparticles. Neural Comput Appl 35(17):12453–12479. https://doi.org/10.1007/s00521-023-08378-3

Al-Fakih A, Mahamood MAA, Al-Osta MA, Ahmad S (2023) Performance and efficiency of self-healing geopolymer technologies: a review. Constr Build Mater 386:131571. https://doi.org/10.1016/j.conbuildmat.2023.131571

Alloun W, Berkani M, Benaissa A, Shavandi A, Gares M, Danesh C, Lakhdari D, Ghfar AA, Chaouche NK (2023) Waste valorization as low-cost media engineering for auxin production from the newly isolated Streptomyces rubrogriseus AW22: model

development. Chemosphere 326:138394. https://doi.org/10.1016/j.chemosphere.2023.138394

Ambikakumari Sanalkumar KU, Lahoti M, Yang EH (2019) Investigating the potential reactivity of fly ash for geopolymerization. Constr Build Mater 225:283–291. https://doi.org/10.1016/j.conbuildmat.2019.07.140

Aouan B, Alehyen S, Fadil M, EL Alouani M, Khabbazi A, Atbir A, Taibi M (2021) Compressive strength optimization of metakaolin-based geopolymer by central composite design. Chemical Data Collections 31:100636. https://doi.org/10.1016/j.cdc.2020.100636

Aouan B, Alehyen S, Fadil M, El Alouani M, Saufi H, El Herradi EH, El Makhoukhi F, Taibi M (2023a) Development and optimization of geopolymer adsorbent for water treatment: application of mixture design approach. J Environ Manage 338:117853. https://doi.org/10.1016/j.jenvman.2023.117853

Aouan B, Alehyen S, Fadil M, El Alouani M, Saufi H, Taibi M (2023b) Characteristics, microstructures, and optimization of the geopolymer paste based on three aluminosilicate materials using a mixture design methodology. Constr Build Mater 384:131475. https://doi.org/10.1016/j.conbuildmat.2023.131475

Aouan B, El Alouani M, Alehyen S, Fadil M, Saufi H, Laghzizil A, Taibi M, Nunzi J-M (2022) Application of central composite design for optimisation of the development of metakaolin based geopolymer as adsorbent for water treatment. Int J Environ Anal Chem. https://doi.org/10.1080/03067319.2022.2070010

Archer de Carvalho T, Gaspar F, Marques AC, Mateus A (2024) Optimization of formulation ratios of geopolymer mortar based on metakaolin and biomass fly ash. Constr Build Mater 412:134846. https://doi.org/10.1016/j.conbuildmat.2023.134846

Aziz ARA, Aziz SA (2018) Application of box Behnken design to optimize the parameters for Kenaf-epoxy as noise absorber. IOP Conf Ser: Mater Sci Eng. https://doi.org/10.1088/1757-899X/454/1/012001

Bajpai R, Choudhary K, Srivastava A, Sangwan KS, Singh M (2020) Environmental impact assessment of fly ash and silica fume based geopolymer concrete. J Clean Prod 254:120147. https://doi.org/10.1016/j.jclepro.2020.120147

Barbosa VFF, MacKenzie KJD, Thaumaturgo C (2000) Synthesis and characterisation of materials based on inorganic polymers of alumina and silica: sodium polysialate polymers. Int J Inorg Mater 2(4):309–317. https://doi.org/10.1016/S1466-6049(00)00041-6

Bhina MR, Liu K-Y, YuHu J-EH, Tsai CT (2024) Effects of fineness modulus variation in preheated sand on geopolymer material properties. Pract Period Struct Des Constr. https://doi.org/10.1061/PPSCFX.SCENG-1457

Bornhauser P, Calzaferri G (1996) Ring-opening vibrations of spherosiloxanes. J Phys Chem 100(6):2035–2044. https://doi.org/10.1021/jp952198t

Bouchenafa O, Hamzaoui R, Bennabi A, Colin J (2019) PCA effect on structure of fly ashes and slag obtained by mechanosynthesis. applications: mechanical performance of substituted paste CEMI + 50% slag /or fly ashes. Constr Build Mater 203:120–133. https://doi.org/10.1016/j.conbuildmat.2019.01.063

Cao VD, Pilehvar S, Salas-Bringas C, Szczotok AM, Valentini L, Carmona M, Rodriguez JF, Kjøniksen A-L (2018) Influence of microcapsule size and shell polarity on thermal and mechanical properties of thermoregulating geopolymer concrete for passive building applications. Energy Convers Manage 164:198–209. https://doi.org/10.1016/j.enconman.2018.02.076

Carrilero MS, Bienvenido R, Sánchez JM, Álvarez M, González A, Marcos M (2002) A SEM and EDS insight into the BUL and BUE differences in the turning processes of AA2024 Al–Cu alloy. Int J Mach Tools Manuf 42(2):215–220. https://doi.org/10.1016/S0890-6955(01)00112-2

Chen K, Wu D, Zhang Z, Pan C, Shen X, Xia L, Zang J (2022) Modeling and optimization of fly ash–slag-based geopolymer using response surface method and its application in soft soil stabilization. Constr Build Mater 315:125723. https://doi.org/10.1016/j.conbuildmat.2021.125723

Davidovits J (1991) Geopolymers. J Therm Anal 37(8):1633–1656. https://doi.org/10.1007/BF01912193

Dong W, Huang Y, Cui A, Ma G (2023) Mix design optimization for fly ash-based geopolymer with mechanical, environmental, and economic objectives using soft computing technology. J Build Eng. https://doi.org/10.1016/j.jobe.2023.106577

Driouich A, El Hassani SA, Hamah Sor N, Zmirli Z, El Harfaoui S, Mydin MAO, Aziz A, Deifalla AF, Chaair H (2023) Mix design optimization of metakaolin-slag-based geopolymer concrete synthesis using RSM. Results in Engineering 20:101573. https://doi.org/10.1016/j.rineng.2023.101573

Duxson P, Mallicoat SW, Lukey GC, Kriven WM, van Deventer JSJ (2007) The effect of alkali and Si/Al ratio on the development of mechanical properties of metakaolin-based geopolymers. Colloids Surf A 292(1):8–20. https://doi.org/10.1016/j.colsurfa.2006.05.044

Emad W, Salih Mohammed A, Kurda R, Ghafor K, Cavaleri L, M.A.Qaidi S, Hassan AMT, Asteris PG (2022) Prediction of concrete materials compressive strength using surrogate models. Structures 46:1243–1267. https://doi.org/10.1016/j.istruc.2022.11.002

Epstein S, Stolper E (1992) Infrared spectroscopy and hydrogen isotope geochemistry of hydrous silicate glasses. Progress Rep. https://doi.org/10.2172/10125268

Ferreira SLC, Bruns RE, Ferreira HS, Matos GD, David JM, Brandão GC, da Silva EGP, Portugal LA, dos Reis PS, Souza AS, dos Santos WNL (2007) Box-Behnken design: an alternative for the optimization of analytical methods. Anal Chim Acta 597(2):179–186. https://doi.org/10.1016/j.aca.2007.07.011

Gaffet E, Bernard F, Niepce J-C, Charlot F, Gras C, Le Caër G, Guichard J-L, Delcroix P, Mocellin A, Tillement O (1999) Some recent developments in mechanical activation and mechanosynthesis. J Mater Chem 9(1):305–314. https://doi.org/10.1039/a804645j

Ghafri EA, Tamimi NA, El-Hassan H, Maraqa MA, Hamouda M (2024) Synthesis and multi-objective optimization of fly ash-slag geopolymer sorbents for heavy metal removal using a hybrid Taguchi-TOPSIS approach. Environ Technol Innov 35:103721. https://doi.org/10.1016/j.eti.2024.103721

Goodarzi F, Sanei H (2009) Plerosphere and its role in reduction of emitted fine fly ash particles from pulverized coal-fired power plants. Fuel 88(2):382–386. https://doi.org/10.1016/j.fuel.2008.08.015

Grabias-Blicharz E, Panek R, Franus M, Franus W (2022) Mechanochemically assisted coal fly ash conversion into zeolite. Materials 15(20):7174. https://doi.org/10.3390/ma15207174

Habert G, d'Espinose de Lacaillerie JB, Roussel N (2011) An environmental evaluation of geopolymer based concrete production: reviewing current research trends. J Clean Prod 19(11):1229–1238. https://doi.org/10.1016/j.jclepro.2011.03.012

Hamzaoui R, Elkedim O, Gaffet E (2004) Milling conditions effect on structure and magnetic properties of mechanically alloyed Fe–10% Ni and Fe–20% Ni alloys. Mater Sci Eng, A 381(1–2):363–371. https://doi.org/10.1016/j.msea.2004.05.008

Han L, Wang J, Liu Z, Zhang Y, Jin Y, Li J, Wang D (2020) Synthesis of fly ash-based self-supported zeolites foam geopolymer via saturated steam treatment. J Hazard Mater. https://doi.org/10.1016/j.jhazmat.2020.122468

Handke M (1986) Vibrational spectra, force constants, and Si–O bond character in calcium silicate crystal structure. Appl Spectrosc 40(6):871–877. https://doi.org/10.1366/0003702864508322

Haque SM, Kabir A, Rahman N, Azmi SNH (2023) Response surface methodology combined Box-Behnken design optimized green kinetic spectrophotometric and HPLC methods to quantify angiotensin receptor blocker valsartan in pharmaceutical formulations. Spectrochimica Acta-Part a: Mol Biomol Spectro. https://doi.org/10.1016/j.saa.2023.122805

Kakasor Ismael Jaf D, Ismael Abdulrahman P, Salih Mohammed A, Kurda R, Qaidi SMA, Asteris PG (2023) Machine learning techniques and multi-scale models to evaluate the impact of silicon dioxide (SiO2) and calcium oxide (CaO) in fly ash on the compressive strength of green concrete. Constr Build Mater 400:132604. https://doi.org/10.1016/j.conbuildmat.2023.132604

Jiang X, Zhang Y, Xiao R, Polaczyk P, Zhang M, Hu W, Bai Y, Huang B (2020) A comparative study on geopolymers synthesized by different classes of fly ash after exposure to elevated temperatures. J Clean Product. https://doi.org/10.1016/j.jclepro.2020.122500

Kanagaraj B, Anand N, Alengaram UJ, Raj RS, Praveen B, Tattukolla K (2022) Performance evaluation on engineering properties and sustainability analysis of high strength geopolymer concrete. J Build Eng 60:105147. https://doi.org/10.1016/j.jobe.2022.105147

Khan HA, Castel A, Khan MSH (2020) Corrosion investigation of fly ash based geopolymer mortar in natural sewer environment and sulphuric acid solution. Corros Sci. https://doi.org/10.1016/j.corsci.2020.108586

Kosor T, Nakić-Alfirević B, Gajović A (2016) Geopolymerization index of fly ash geopolymers. Vib Spectrosc 85:104–111. https://doi.org/10.1016/j.vibspec.2016.04.005

Lecomte I, Liégeois M, Rulmont A, Cloots R, Maseri F (2003) Synthesis and characterization of new inorganic polymeric composites based on kaolin or white clay and on ground-granulated blast furnace slag. J Mater Res 18(11):2571–2579. https://doi.org/10.1557/JMR.2003.0360

Liu Y, Yan C, Zhang Z, Wang H, Zhou S, Zhou W (2016) A comparative study on fly ash, geopolymer and faujasite block for Pb removal from aqueous solution. Fuel 185:181–189. https://doi.org/10.1016/j.fuel.2016.07.116

Luan C, Zhou M, Zhou T, Wang J, Yuan L, Zhang K, Ren Z, Liu Y, Zhou Z (2022) Optimizing the design proportion of high-performance concrete via using response surface method. Iran J Sci Technol Trans Civil Eng 46(4):2907–2921. https://doi.org/10.1007/s40996-021-00802-9

Luo Y, Klima KM, Brouwers HJH, Yu Q (2022) Effects of ladle slag on class F fly ash geopolymer: reaction mechanism and high temperature behavior. Cement Concr Compos. https://doi.org/10.1016/j.cemconcomp.2022.104468

Mahfoud E, Maherzi W, Ndiaye K, Benzerzour M, Aggoun S, Abriak NE (2023) Mechanical and microstructural properties of just add water geopolymer cement comprised of thermo-mechanicalsynthesis sediments-fly ash mix. Constr Build Mater. https://doi.org/10.1016/j.conbuildmat.2023.132626

Martínez A, Miller SA (2023) A review of drivers for implementing geopolymers in construction: codes and constructability. Resour Conserv Recycl. https://doi.org/10.1016/j.resconrec.2023.107238

Mozgawa W, Król M, Dyczek J, Deja J (2014) Investigation of the coal fly ashes using IR spectroscopy. Spectrochim Acta Part A Mol Biomol Spectrosc 132:889–894. https://doi.org/10.1016/j.saa.2014.05.052

Mucsi G, Kumar S, Csoke B, Kumar R, Molnár Z, Rácz Á, Mádai F, Debreczeni Á (2015) Control of geopolymer properties by grinding of land filled fly ash. Int J Miner Process 143:50–58. https://doi.org/10.1016/j.minpro.2015.08.010

Murmu AL, Dhole N, Patel A (2020) Stabilisation of black cotton soil for subgrade application using fly ash geopolymer. Road Mater Pavement Des 21(3):867–885. https://doi.org/10.1080/14680629.2018.1530131

Nada MH, Larsen SC, Gillan EG (2019) Mechanochemically-assisted solvent-free and template-free synthesis of zeolites ZSM-5 and mordenite. Nanoscale Advances 1(10):3918–3928. https://doi.org/10.1039/c9na00399a

Nath SK, Kumar S (2020) Role of particle fineness on engineering properties and microstructure of fly ash derived geopolymer. Constr Build Mater. https://doi.org/10.1016/j.conbuildmat.2019.117294

Nawaz M, Heitor A, Sivakumar M (2020) Geopolymers in construction - recent developments. Constr Build Mater 260:120472. https://doi.org/10.1016/j.conbuildmat.2020.120472

Ndlovu NZN, Missengue RNM, Petrik LF, Ojumu T (2017) Synthesis and characterization of faujasite zeolite and geopolymer from South African coal fly ash. J Environ Eng. https://doi.org/10.1061/(asce)ee.1943-7870.0001212

Özkılıç YO, Karalar M, Aksoylu C, Beskopylny AN, Stelmakh SA, Shcherban EM, Qaidi S, da Pereira Iully SA, Monteiro SN, Azevedo ARG (2023) Shear performance of reinforced expansive concrete beams utilizing aluminium waste. J Mater Res Technol 24:5433–5448. https://doi.org/10.1016/j.jmrt.2023.04.120

Pan Z, Tan M, Zheng G, Wei L, Tao Z, Hao Y (2024) Effect of silica fume type on rheology and compressive strength of geopolymer mortar. Constr Build Mater 430:136488. https://doi.org/10.1016/j.conbuildmat.2024.136488

Panda S, Pradhan M, Panigrahi SK (2024) Optimal red mud replacement level evaluation in conventional concrete based on fresh and hardened concrete characteristics. J Sustain Metall 10(2):835–850. https://doi.org/10.1007/s40831-024-00837-y

Parhi SK, Dwibedy S, Panigrahi SK (2024) AI-driven critical parameter optimization of sustainable self-compacting geopolymer concrete. J Build Eng 86:108923. https://doi.org/10.1016/j.jobe.2024.108923

Payakaniti P, Chuewangkam N, Yensano R, Pinitsoontorn S, Chindaprasirt P (2020) Changes in compressive strength, microstructure and magnetic properties of a high-calcium fly ash geopolymer subjected to high temperatures. Constr Build Mater. https://doi.org/10.1016/j.conbuildmat.2020.120650

Phair JW, Van Deventer JSJ (2002) Effect of the silicate activator pH on the microstructural characteristics of waste-based geopolymers. Int J Miner Process 66(1–4):121–143. https://doi.org/10.1016/S0301-7516(02)00013-3

Pradhan J, Panda S, Dwibedy S, Pradhan P, Panigrahi SK (2024a) Production of durable high-strength self-compacting geopolymer concrete with GGBFS as a precursor. J Mater Cycles Waste Manage 26(1):529–551. https://doi.org/10.1007/s10163-023-01851-0

Pradhan J, Panda S, Parhi SK, Pradhan P, Panigrahi SK (2024b) GGBFS-based self-compacting geopolymer concrete with optimized mix parameters established on fresh, mechanical, and durability characteristics. J Mater Civil Eng. https://doi.org/10.1061/JMCEE7.MTENG-16669

Puertas F, Palacios M, Vázquez T (2006) Carbonation process of alkali-activated slag mortars. J Mater Sci 41(10):3071–3082. https://doi.org/10.1007/s10853-005-1821-2

Rahimzadeh CY, Mohammed AS, Barzanji AA (2024) Optimizing building insulation with silica nanoparticles: a study on lime-based roof and screed pastes for enhanced compressive strength and thermogravimetric analysis. Eur J Environ Civil Eng. https://doi.org/10.1080/19648189.2024.2324097

Rathee M, Misra A, Kolleboyina J, Sarma P, S. K. (2023) Study of mechanical properties of geopolymer mortar prepared with fly ash and GGBS. Mater Today: Proc 93:377–386. https://doi.org/10.1016/j.matpr.2023.07.360

Rodrigue Kaze C, Ninla Lemougna P, Alomayri T, Assaedi H, Adesina A, Kumar Das S, Lecomte-Nana G-L, Kamseu E, Chinje Melo U, Leonelli C (2021) Characterization and performance evaluation of laterite based geopolymer binder cured at different temperatures. Constr Build Mater 270:121443. https://doi.org/10.1016/j.conbuildmat.2020.121443

Ryu GS, Lee YB, Koh KT, Chung YS (2013) The mechanical properties of fly ash-based geopolymer concrete with alkaline activators. Constr Build Mater 47:409–418. https://doi.org/10.1016/j.conbuildmat.2013.05.069

Samouh H, Kumar V, Santiago HM, Garg N (2023) Enhancing phase identification in waste-to-energy fly ashes: role of Raman spectroscopy, background fluorescence, and photobleaching. J Hazard Mater. https://doi.org/10.1016/j.jhazmat.2023.132462

Sathsarani HBS, Sampath KHSM, Ranathunga AS (2023) Utilization of fly ash-based geopolymer for well cement during CO2 sequestration: A comprehensive review and a meta-analysis. Gas Sci Eng. https://doi.org/10.1016/j.jgsce.2023.204974

Shi X, Zhang C, Wang X, Zhang T, Wang Q (2022) Response surface methodology for multi-objective optimization of fly ash-GGBS based geopolymer mortar. Constr Build Mater. https://doi.org/10.1016/j.conbuildmat.2021.125644

Shilar FA, Ganachari SV, Patil VB, Khan TMY, Dawood Abdul Khadar S (2022) Molarity activity effect on mechanical and microstructure properties of geopolymer concrete: a review. Case Stud Constr Mater. https://doi.org/10.1016/j.cscm.2022.e01014

Singh NB, Middendorf B (2020) Geopolymers as an alternative to Portland cement: an overview. Constr Build Mater 237:117455. https://doi.org/10.1016/j.conbuildmat.2019.117455

Šontevska V, Jovanovski G, Makreski P (2007) Minerals from Macedonia. Part XIX. Vibrational spectroscopy as identificational tool for some sheet silicate minerals. J Mol Struct 834–836:318–327. https://doi.org/10.1016/j.molstruc.2006.10.026

Srinivasa AS, Swaminathan K, Yaragal SC (2023) Microstructural and optimization studies on novel one-part geopolymer pastes by Box-Behnken response surface design method. Case Stud Constr Mater 18:e01946. https://doi.org/10.1016/j.cscm.2023.e01946

Tang J, Liu P, Shang J, Fei Y (2023) Application of CO2-loaded geopolymer in Zn removal from water: a multi-win strategy for coal fly ash disposal, CO2 emission reduction, and heavy metal-contaminated water treatment. Environ Res. https://doi.org/10.1016/j.envres.2023.117012

Tchadjie LN, Ekolu SO (2018) Enhancing the reactivity of aluminosilicate materials toward geopolymer synthesis. J Mater. https://doi.org/10.1007/s10853-017-1907-7

Tchakouté HK, Rüscher CH, Hinsch M, Djobo JNY, Kamseu E, Leonelli C (2017) Utilization of sodium waterglass from sugar cane bagasse ash as a new alternative hardener for producing metakaolin-based geopolymer cement. Geochemistry 77(2):257–266. https://doi.org/10.1016/j.chemer.2017.04.003

Van Jaarsveld JGS, Van Deventer JSJ (1999) Effect of the alkali metal activator on the properties of fly ash-based geopolymers. Ind Eng Chem Res 38(10):3932–3941. https://doi.org/10.1021/ie980804b

Wang YC, Zhang YJ, Xu Y, Xu DL (2011) Study on performance of alkali-activated flyash-based geopolymer reinforced by silica fume and styrene-acrylic emulsion. Adv Mater Res 374–377:1632–1636. https://doi.org/10.4028/www.scientific.net/AMR.374-377.1632

Wang T, Fan X, Gao C (2024) Development of high-strength geopolymer mortar based on fly ash-slag: correlational analysis of microstructural and mechanical properties and environmental assessment. Constr Build Mater 441:137515. https://doi.org/10.1016/j.conbuildmat.2024.137515

Wang X, Fan T (2021) Optimization in process parameters of calcium sulfate whisker modified asphalt using response surface methodology. Iran J of Sci Technol Trans Civil Eng 45(4):2841–2851. https://doi.org/10.1007/s40996-020-00549-9

Yan W, Liu D, Tan D, Yuan P, Chen M (2012) FTIR spectroscopy study of the structure changes of palygorskite under heating. Spectrochim Acta Part A Mol Biomol Spectrosc 97:1052–1057. https://doi.org/10.1016/j.saa.2012.07.085

Yang C, You J-J, Huang Y-W, Ji X-M, Song Q-Y, Liu Q (2023) Low-carbon enhancement of fly ash geopolymer concrete: Lateral deformation, microstructure evolution and environmental impact. J Clean Prod 422:138610. https://doi.org/10.1016/j.jclepro.2023.138610

Yong-Jie H, Cheng-Yong H, Yun-Ming L, Abdullah MMAB, Yeng-Seng L, Wei-Hao L, Pakawanit P, Shee-Ween O, Hoe-Woon T, Cheng-Hsuan H (2024) Microwave absorption function on a novel one-part binary geopolymer: Influence of frequency, ageing and mix design. Constr Build Mater 427:136264. https://doi.org/10.1016/j.conbuildmat.2024.136264

Zerzouri M, Bouchenafa O, Hamzaoui R, Ziyani L, Alehyen S (2021) Physico-chemical and mechanical properties of fly ash based-geopolymer pastes produced from pre-geopolymer powders obtained by mechanosynthesis. Constr Build Mater 288:123135. https://doi.org/10.1016/j.conbuildmat.2021.123135

Zerzouri M, Hamzaoui R, Ziyani L, Alehyen S (2022) Influence of slag based pre-geopolymer powders obtained by mechanosynthesis on structure, microstructure and mechanical performance of geopolymer pastes. Constr Build Mater. https://doi.org/10.1016/j.conbuildmat.2022.129637

Zhang D-W, Sun X-M, Li H (2023a) Relationship between macro-properties and amorphous gel of FA-based AAMs with different curing conditions after elevated temperature. Ceram Int 49(11):17453–17467. https://doi.org/10.1016/j.ceramint.2023.02.113

Zhang J, Fu Y, Wang A, Dong B (2023b) Research on the mechanical properties and microstructure of fly ash-based geopolymers modified by molybdenum tailings. Constr Build Mater. https://doi.org/10.1016/j.conbuildmat.2023.131530

Ziegler D, Formia A, Tulliani JM, Palmero P (2016) Environmentally-friendly dense and porous geopolymers using fly ash and rice husk ash as raw materials. Materials. https://doi.org/10.3390/ma9060466